WILEY-VCH

DOI: 10.1002/
Article type: Full Paper

Boosting Photoelectrochemical Water Oxidation of Hematite in Acidic Electrolytes by Surface States Modification

Peng-Yi Tang, Li-Juan Han, Franziska Simone Hegner, Paul Paciok, Martí Biset-Peiró, Hong-Chu Du, Xian-Kui Wei, Lei Jin, Hai-Bing Xie, Qin Shi, Teresa Andreu, Mónica Lira-Cantú, Marc Heggen, Rafal E. Dunin-Borkowski, Núria López, José Ramón Galán-Mascarós, Joan Ramon Morante, Jordi Arbiol**

Dr. P. Y. Tang, Dr. H. B. Xie, Dr. M. Lira-Cantú, Prof. J. Arbiol
Catalan Institute of Nanoscience and Nanotechnology (ICN2), CSIC and BIST, Campus UAB, Bellaterra, 08193 Barcelona, Catalonia, Spain
E-mail: arbiol@icrea.cat

Dr. P. Y. Tang, M. Biset-Peiró, Dr. Q. Shi, Dr. T. Andreu, Prof. J. R. Morante
Catalonia Institute for Energy Research (IREC), Jardins de les Dones de Negre 1, Sant Adrià del Besòs, Barcelona 08930, Catalonia, Spain
E-mail: jrmorante@irec.cat

L. J. Han, Dr. F. S. Hegner, Prof. N. López, Prof. J. R. Galán-Mascarós
Institute of Chemical Research of Catalonia (ICIQ), BIST, Avinguda Països Catalans 16, Tarragona 43007, Catalonia, Spain

Dr. P. Paciok, Dr. H. C. Du, Dr. X. K. Wei, Dr. L. Jin, Dr. M. Heggen, Prof. R. E. Dunin-Borkowski
Ernst-Ruska Centre for Microscopy and Spectroscopy with Electrons and Peter Grünberg Institute, Forschungszentrum Jülich GmbH, 52425 Jülich, Germany

Prof. J. R. Galán-Mascarós, Prof. J. Arbiol
ICREA, Pg. Lluís Companys 23, 08010 Barcelona, Catalonia, Spain.

State-of-the-art water-oxidation catalysts in acidic electrolyte usually contain expensive noble metals such as ruthenium and iridium. However, they are exceedingly expensive to be implemented broadly in semiconductor photoanodes for affordable photoelectrochemical (PEC) water splitting devices. Here, an Earth-abundant CoFe Prussian blue analogue (CoFe-PBA) is incorporated with core-shell Fe_2O_3/Fe_2TiO_5 type II heterojunction nanowires as composite photoanodes for PEC water splitting. Those deliver a high photocurrent of 1.25 mA cm^{-2} at 1.23 V vs. reversible reference electrode in acidic electrolyte (pH=1). The enhancement arises from the synergic behavior between the successive decoration of the hematite surface with nanolayers of Fe_2TiO_5 and then, CoFe-PBA. The underlying physical mechanism of performance enhancement through formation of the Fe_2O_3/Fe_2TiO_5/CoFe-PBA heterostructure reveals that the surface states electronic levels of hematite were modified such that an interfacial charge transfer becomes kinetically favorable. These findings open new pathways for the future design of cheap and efficient hematite-based photoanodes in acidic electrolytes.

1. Introduction

Photoelectrochemical (PEC) water splitting devices, using Earth-abundant semiconductor materials, have long been considered to be the ‘‘Holy Grail’’ of solar energy conversion.[1-9] For the design of a beneficial device structure, in which both electrodes are exposed to the same medium, and considering that the hydrogen evolution is most efficiently carried out in acidic electrolyte and the advantages of the proton exchange membrane (PEM), a robust photoanode would be highly desirable.[10-15] Nonetheless the development of an efficient and affordable photoanode, which is stable in acidic electrolyte, imposes a great challenge and limits the large-scale implementation of economically viable PEC water-splitting. In light of this challenge, much attention has been drawn to the development of efficient and affordable photoanode systems adapted to acidic electrolytes.

Hematite is arguably the most desirable photoanode material. On one hand, its relatively small bandgap of 1.9-2.1 eV and suitably aligned valence band level perfectly match the thermodynamic energy requirements needed to drive water oxidation.[4, 10] On the other hand, it is made from the most abundant transition metal on Earth crust, iron. Unfortunately, the bare hematite surface is catalytically very poor, and therefore requires significant modifications with water-oxidation catalysts (WOCs) in order to extract the thermodynamic power stored when light is absorbed.

Regarding efficient WOCs in acidic electrolyte, many researchers have hitherto devoted their efforts to explore cheap, effective alternatives to the state-of-the-art ruthenium (Ru) and iridium (Ir) based WOCs.[14-18] For example, cobalt-containing polyoxometalates (Co-POMs),[16] Ti-stabilized MnO_2,[19] $W_{1-x}Ir_xO_{3-\delta}$,[20] $Ni_xMn_{1-x}Sb_{1.6-1.8}O_y$,[21] Fe-$TiO_x$,[22] iron (III) oxide,[23] cobalt-doped hematite,[24] and cobalt-iron Prussian blue analogue (CoFe-PBA)[25-26] WOCs have been substantially explored. For a successful WOC-functionalized photoanode, it is necessary to consider the utilization of light capture of semiconductors and the catalytic effect of WOCs simultaneously, that is to say, boosting the performance of the WOCs without compromising the light absorption features.[11-12] Up to date, few reports have appeared on smart integration of hematite with WOCs, and most of them related to noble Ir-based catalysts,[11, 27-29] with which a maximum photocurrent response of 0.66 mA cm^{-2} at 1.23 V *vs.* reversible reference electrode (RHE) in acidic electrolyte (pH = 1.01) was obtained.[11] Thus, even by coupling with noble Ir-based WOCs, the photocurrent response of hematite based photoanodes in acidic electrolyte remains much lower than its theoretical value (12.5 mA cm^{-2}).[30]

Meanwhile, it is well established that the surface states present in the bandgap of hematite, mediates hole transfer and plays a vital role in determining its PEC performance.[31-32] There are two types of surface states, intrinsic surface states derived from the loss of translational bulk crystal symmetry, and extrinsic surface states due to chemical bond formation/surface

interaction with a secondary species.[33-34] While it is difficult to completely remove intrinsic surface states, they can be modified by depositing a secondary species,[35] which has recently been demonstrated.[28, 36-38] For instance, our previous investigation about ITO/Fe_2O_3/Fe_2TiO_5/ FeNiOOH photoanodes in alkaline electrolytes reveals that the surface states of hematite can be modified by atomic layer deposited Fe_2TiO_5 and photo-electrodeposited FeNiOOH.[38] Moreover, hematite photoanodes were combined with a CoFe-PBA resulting in enhanced photocurrent response in neutral electrolyte.[37] Despite these observations in neutral and alkaline electrolytes, rare reports on the performance of hematite-based photoanodes in acidic media have been published, despite the extraordinary technological interest, as described above.

With the aim of designing cheap and efficient hematite based photoanodes in acidic electrolyte, we decided to merge these two previous strategies. Firstly, we fabricated core-shell Fe_2O_3/ Fe_2TiO_5 type II heterostructured nanowires, as a surface-modification approach to enhance photocatalytic activity. Secondly, we decorated these nanowires with a nanolayer of an acid-stable WOC, the CoFe-PBA (Scheme S1). These photoanodes were prepared on fluoride-doped tin oxide (FTO) glass electrodes in three steps: hydrothermal deposition of Fe_2O_3; atomic layer deposition (ALD) of Fe_2TiO_5; and finally, chemical bath deposition of CoFe-PBA; as displayed in **Figure 1**A. These heterostructures are able to produce the highest photocurrent response in acid media ever observed for a hematite-based photoanode, when made by scalable processes, and earth-abundant materials, opening new strategies for hematite-based PEC water splitting in acidic electrolyte.

2. Results and Discussion

2.1. Processing and structural characterization

Vertically aligned Fe_2O_3 nanowires with diameters ranging from 100 to 200 nm (**Figure 1**B) were firstly grown on a FTO substrate via a hydrothermal method.[38] Then, a thin TiO_2 layer was coated onto the Fe_2O_3 nanowires by 30 ALD cycles. The surface coated TiO_2 was

subsequently transformed into Fe_2TiO_5 through a post-sintering process in ambient atmosphere at 750 ºC for 30 min. As displayed in **Figure 1**C, the Fe_2O_3/Fe_2TiO_5 heterostructured nanowires are homogeneous without changing the nanowire-like architecture. Subsequently, the obtained Fe_2O_3/Fe_2TiO_5 composite nanowires were subjected to a chemical bath for 2h in the presence of the CoFe-PBA precursor at 60 ℃ to produce Fe_2O_3/Fe_2TiO_5/CoFe-PBA heterostructured nanowires. Its SEM image in **Figure** 1D reveals that the diameter of these nanowires did not change compared to the Fe_2O_3/Fe_2TiO_5 ones, indicating the ultrathin CoFe-PBA coating. The sample crystallinity and chemical composition were further analyzed via energy dispersive X-ray spectroscopy (EDX), X-ray photoelectron spectroscopy (XPS) and X-ray diffraction (XRD), Raman spectrum and FT-IR spectrum in Figures S1-S5, evidencing the existence of hematite, Fe_2TiO_5 and CoFe-PBA species in the corresponding electrodes.

The structure, crystallography and spatial distribution of hematite, Fe_2TiO_5 and CoFe-PBA species were further investigated by aberration-corrected scanning transmission electron microscopy (AC-STEM) in high angle annular dark-field (HAADF) mode. On one hand, the HAADF STEM images of Fe_2O_3 and Fe_2O_3/Fe_2TiO_5 electrodes on the top and middle rows of **Figure 2** show the atomic ordering of the hematite matrix. On the other hand, the Fe_2TiO_5 species in the Fe_2O_3/Fe_2TiO_5 electrode are shown as a blurred ultrathin shell on the surface of the hematite nanowires (middle rows of **Figure 2** and Figure S10), in good agreement with the maps obtained by STEM combined with electron energy loss spectroscopy (EELS) in Figure S12 conducted on the same region. The additional atomic resolution HAADF STEM imaging in combination with the STEM-EELS compositional maps of the Fe_2O_3 and Fe_2O_3/Fe_2TiO_5 electrodes are included in Figures S6-S12, confirming the core-shell nanowires structure of the Fe_2O_3/Fe_2TiO_5 electrode. Notably, coordination polymers are especially susceptible to the electron beam damage, hindering stable atomic-level HAADF

STEM observation of the CoFe-PBA.[25, 38-41] Thus, we employed bright field HRTEM to monitor the surface structure evolution of the Fe_2O_3/Fe_2TiO_5/CoFe-PBA electrodes.

Figure 2A displays a representative TEM image of a Fe_2O_3/Fe_2TiO_5/CoFe-PBA nanowire. According to **Figures 2**B-D, the nanoparticles attached to the composite nanowire can be assigned to CoFe-PBA species. The hematite and Fe_2TiO_5 phases dominate the nanowires matrix, as identified by the HRTEM and its corresponding power spectrum in **Figures 2**E-F. Moreover, the corresponding frequency filtered image (**Figure 2**G) clearly illustrates the presence of a localized hematite nanowire core and an ultrathin pseudo-brookite shell. **Figure 2**E and Figure S13 show that the fine CoFe-PBA shell on the nanowires surface tends to possess an amorphous structure, whereas bigger CoFe-PBA nanoparticles present lattice fringes denoting its good crystallinity, as displayed in **Figures 2**C and Figure S14.

The spatial elemental distribution of Fe_2O_3/Fe_2TiO_5/CoFe-PBA electrodes was further characterized via HAADF STEM combined with EELS. In addition to the elemental signals from the CoFe-PBA nanoparticles, we also found the presence of C, N, O, Co and Fe surrounding the nanowire matrix in the STEM-EELS maps shown in **Figure** 3 and Figures S15-S16.[25] These results evidence that the surface amorphous region observed in **Figure 2**E is indeed an ultrathin CoFe-PBA shell at the surface of the Fe_2O_3/Fe_2TiO_5 nanowires. Addtionally, the statistical diameter size distributions of Fe_2O_3, Fe_2O_3/Fe_2TiO_5 and Fe_2O_3/Fe_2TiO_5/CoFe PBA nanowires in Figure S17 reveals that Fe_2O_3, Fe_2O_3/Fe_2TiO_5, Fe_2O_3/Fe_2TiO_5/CoFe PBA nanowires have average diameter size of 168 ± 43 nm, 174 ± 63 nm and 185 ± 70 nm, respectively. The average diameter size of these nanowires did not significantly change with the coating of Fe_2TiO_5 and CoFe PBA, which is consistent with the SEM results.

2.2. Photoelectrochemical performance

The detailed PEC performance measured for these photoanodes is displayed in **Figure 4**. Cyclic voltammtry (CV) measurements in the dark (**Figure 4**A) show a positive shift of the

onset potential of hematite upon coating with the ultrathin Fe_2TiO_5 shell, consistent with our previous work,[38] whereas modification with CoFe-PBA reduces the onset potential of the Fe_2O_3/ Fe_2TiO_5 electrode, which demonstrates the positive catalytic effect of CoFe-PBA. Under light irradiation, the CV in **Figure 4**B and the statistical data in Figure S18 reveal that pristine Fe_2O_3 electrodes exhibits a very low photocurrent response of 0.12 mA cm^{-2} at 1.23 V *vs.* RHE, the thermodynamic potential for the oxygen evolution reaction (OER).[42] Upon Fe_2TiO_5 deposition, the photocurrent density increases significantly above 1.0 V *vs.* RHE, reaching 0.90 mA cm^{-2} at 1.23 V *vs.* RHE (**Figure 4**B). The onset potential is further improved in the Fe_2O_3/Fe_2TiO_5/CoFe-PBA electrode. This parameter was used to optimize the Fe_2O_3/Fe_2TiO_5/ CoFe-PBA processing (Figures S19-S20). According to the statistical data in Figure S19, we reached a maximum PEC performance with electrodes coated with CoFe-PBA by a chemical bath reaction at 60 ℃ for 2h, giving 1.25 mA cm^{-2} at 1.23 V *vs.* RHE. To the best of our knowledge, this is the highest photocurrent value observed for hematite-based photoanodes in acidic electrolyte (see Table S1). Moreover, it is better than the photocurrent response for Fe_2O_3/Fe_2TiO_5 (0.90 mA cm^{-2}, **Figure 4**B) and Fe_2O_3/CoFe-PBA (0.62 mA cm^{-2}, based on the statistical data in Figures S21-S22) electrodes indicating a synergic effect in combining core-shell Fe_2O_3/Fe_2TiO_5 type II heterojunction with the CoFe-PBA WOC.

The chopped light photocurrent-potential curves in **Figure 4**C show smaller photocurrent transients for the Fe_2O_3/Fe_2TiO_5/CoFe-PBA electrodes, in particular in the potential range of 1.2-1.7 V vs. RHE. This reduction of the photocurrent transient indicates that the electron-hole recombination is suppressed by the Fe_2TiO_5 and CoFe-PBA modification, further demonstrating its advantage. Moreover, the UV-vis absorptance, Tauc plots, IPCE, and APCE spectra of the Fe_2O_3, Fe_2O_3/Fe_2TiO_5, and Fe_2O_3/Fe_2TiO_5/CoFe PBA electrodes in Figure S23 further evidence that the enhanced PEC performance of Fe_2O_3/Fe_2TiO_5/CoFe-PBA electrodes is attributed to the synergetic effect from Fe_2TiO_5 and CoFe-PBA.

The PEC stability of these three electrodes was investigated by chronoamperometry at a constant applied working potential of 1.23 V *vs.* RHE (**Figure 4**D) at pH = 1 for 24 h. The photocurrent response of Fe_2O_3 electrodes shows a slow but continuous decrease, maintaining about 40% of the initial photocurrent response after 24 h test. In contrast, Fe_2O_3/Fe_2TiO_5 electrodes and Fe_2O_3/Fe_2TiO_5/CoFe-PBA electrodes follow a similar trend, showing an initial drop in photocurrent during the first 2 h and show no further sign of fatigue during the rest stability measurement, retaining around 80% of the initial photocurrent response after 24 h test. Additionally, we monitored the evolved oxygen in the case of Fe_2O_3/Fe_2TiO_5/CoFe-PBA electrodes by a calibrated Fibox O_2 detector in a gastight cell during the first 2 h water oxidation at 1.23 V vs RHE. (Figure S24A). The theoretical oxygen yield was calculated from the total charge passed during PEC water oxidation. Faradaic Efficiencies above 94% were demonstrated (Figure S24B), indicating that the photocurrent response is mainly originating from the water oxidation process. The enhanced stability of Fe_2O_3/Fe_2TiO_5, and Fe_2O_3/Fe_2TiO_5/ CoFe-PBA electrode compared to Fe_2O_3 electrode is further confirmed by the CV curves of these electrodes after 24 h stability test in Figure S25. Moreover, the SEM images of Fe_2O_3 electrodes after 24 h stability measurement in Figure S26A-C reveal that the attenuation of the photocurrent response in Fe_2O_3 electrodes is derived from its nanowires structure degradation in acidic electrolyte. Meanwhile, the degradation of Fe_2O_3/Fe_2TiO_5, and Fe_2O_3/Fe_2TiO_5/CoFe-PBA electrodes' nanowires are substantially suppressed, as displayed in Figure S26D-I. Therefore, we assign the drastically enhanced stability of Fe_2O_3/Fe_2TiO_5/ CoFe-PBA electrodes to the dual protective effect provided by the Fe_2TiO_5 and the CoFe-PBA (Figure 4E), both of which are stable in acidic electrolytes. [19, 22, 25, 43]

2.3. Mechanistic investigation via PEIS

It is well established that the catalytic activity of photoanodes is strongly dependent on the characteristics of the surface states at the semiconductor-electrolyte interface (SEI).[44-46] While those surface states can limit water oxidation kinetics by acting as electron-hole

recombination centers, they can also have a beneficial influence on water oxidation, promoting electron transfer across the interface, dependent on their respective kinetics.[47] In particular, electrical active surface states presented in the hematite bandgap are supposed to play a vital role in PEC water oxidation, thus, a deeper investigation is required to probe their effect on charge transfer at the SEI (**Figure 4**E).[38, 48-51]

We employed CV and PEIS techniques to monitor the evolution of such surface states in hematite,[44-45] which was suggested to be an iron-oxo intermediate by in operando IR spectroscopy[48] and density functional theory calculations[52-53] and how it is influenced by successive Fe_2TiO_5 and CoFe-PBA deposition. As displayed in **Figure 5**A, the precatalytic feature in the CV, which is related to adding and removing electrons to/from the surface states, changes with the addition of Fe_2TiO_5 and CoFe-PBA.[48] Their significant impact on the surface states was further suggested by PEIS. The equivalent circuits in Figure S29 were used to fit the obtained data in Figures S27-S28; the obtained resistances and capacitances are shown in Figures S30-S31.

From the fitted surface states or trap capacitance C_{trap}, we estimated the density of surface states (DOSS) with equation (1):[32, 36, 54-55]

$$\mathrm{N_{SS}(E)} = \frac{\mathrm{C_{trap}(E)}}{\mathrm{q}}(1) N_{SS}\ (\mathrm{E}) =$$

$$\frac{C_{trap}(\mathrm{E})}{\mathrm{q}} \qquad (1)$$

Where N_{ss} (E) is the DOSS ($cm^{-2}\ eV^{-1}$) as a function of the applied potential and q is the electron charge (1.602×10^{-19} C). As shown in **Figure 5**B, the energy and density distribution of the surface states N_{ss}[32, 54] follows the order $Fe_2O_3 < Fe_2O_3/Fe_2TiO_5 < Fe_2O_3/Fe_2TiO_5$/ CoFe-PBA across the entire surface states dominated region (0.86 V to 1.46 V). The extended surface states distribution from 0.86 V to 1.46 V in unmodified Fe_2O_3 electrodes probably spans inside the CB, where recombination with CB electrons may occur. Moreover, it triggers a deleterious Fermi level pinning, which also contributes to its low photocurrent response.[54]

Upon surface modification, the DOSS maximum shifts to more positive potentials, i.e. further into the bandgap, which minimizes overlap with the conduction band (**Figure 5**C). Further, its shape coincides well with the cathodic CV curves obtained after holding the electrodes at a potential of 1.85 V *vs*. RHE for 1 min (**Figure 5**A), which also indicates the correct utilization of the equivalent circuit model for PEIS fitting.[44, 48] Consequently, the ultrathin Fe_2TiO_5 and CoFe-PBA coatings indeed work together modifying the density and energy level of the surface state in hematite photoanodes.

Assuming surface states mediated charge-transfer (CT), the CT rate constant (k_{ct}) at a certain electrode polarization potential (E), is proportional to equation (2):[28, 32, 54-56]

$$k_{ct} \propto \int_{E_{v,s}}^{E} N_{ss} f(E) D_{H_2O}(E) dE \qquad (2)$$

in which f(E) is the Fermi-Dirac distribution indicating the fraction of occupied surface states and D_{H2O}(E) is the water density of states ($cm^{-2}eV^{-1}$). Given that the inelastic hole trapping process mediated by surface states is fast enough,[53] the photocurrent response is proportional to k_{ct},[57] depending on the overlap between the filled surface states and the filled water density of states. There is thus, a direct correlation between the percentage of available filled surface states (larger DOSS) near the thermodynamic potential for water oxidation and the observed photocurrent response at 1.23 V *vs.* RHE because of the required isoenergetic hole transfer process at the SEI.[38, 54-55] As illustrated in **Figure 5**C, the Fe_2O_3/Fe_2TiO_5/CoFe-PBA electrode possesses the highest photocurrent response at 1.23 V *vs.* RHE due to the maximum energy level matching between the surface states of the photoanodes and the water density of states.

Furthermore, a combined comparison of the N_{ss}, N_d and N_{ss}/N_d ratio is presented in **Figure 5**D. The pristine Fe_2O_3 electrodes present a relatively high N_{ss}/N_d ratio but poor PEC performance, indicating that a large N_{ss}/N_d ratio does not guarantee a good photocurrent response due to the lack of donors and low electrical conductivity. For the Fe_2O_3/Fe_2TiO_5 electrodes, the N_d is

promoted via Ti doping, and this enables a higher photocurrent. In the case of the Fe_2O_3/Fe_2TiO_5/CoFe-PBA electrode, N_{ss} and N_d are both numerous enough to further increase the photocurrent response.

The charge transfer efficiency at the SEI is firstly estimated by (equation (3)):[33, 54, 57-58]

$$\text{Transfer efficiency}(\%) = \frac{k_{ct}}{k_{ct}+k_{trapping}} = \frac{R_{trapping}}{\mathrm{R_{ct,trap}}+\mathrm{R_{trapping}}} \quad (3)$$

where k_{ct} and $k_{trapping}$ are the charge transfer and trapping rate constants, respectively, and R_{ct} and $R_{trapping}$ are the corresponding resistances. The calculated charge transfer efficiency from PEIS is shown in **Figure 5**E. In the case of the Fe_2O_3/Fe_2TiO_5/CoFe-PBA electrode, over 60% of the holes are transferred into the electrolyte at 1.23 V *vs.* RHE, which is almost 10 times as high as for pristine Fe_2O_3. Additionally, the calculated charge transfer efficiency of these electrodes is in good agreement with the steady-state current-voltage relationship (**Figure 4**B) and the charge separation efficiencies (Figure S32) of Fe_2O_3, Fe_2O_3/Fe_2TiO_5 and Fe_2O_3/Fe_2TiO_5/CoFe-PBA electrodes obtained via comparing the cyclic voltammetry measurements in electrolyte with hole scavenger and without hole scavenger, further confirming the highest charge transfer efficiency of the Fe_2O_3/Fe_2TiO_5/CoFe-PBA electrodes. [32]

3. Conclusion

In summary, we have successfully integrated Fe_2O_3 nanowires with an ultrathin Fe_2TiO_5 heterojunction and CoFe-PBA decoration for enhanced PEC water splitting in acid electrolyte (pH = 1). Thanks to the combination of core-shell Fe_2O_3/Fe_2TiO_5 type II heterojunction nanowires and the catalytic function of CoFe-PBA, Fe_2O_3/Fe_2TiO_5/CoFe-PBA composite photoanodes are able to deliver 1.25 mA cm^{-2} photocurrent at 1.23 V *vs.* RHE, almost one order of magnitude photocurrent increment in comparison to the pristine Fe_2O_3 nanowires. By a systematic electrochemical investigation, the enhanced PEC performance of the Fe_2O_3/Fe_2TiO_5/CoFe-PBA composite electrode can be attributed to the modified surface states

density after successive coatings as well as the enhanced donor density derived from inevitable Ti doping during the high temperature sintering.[38] This work suggests that simultaneously employing the synergy of core-shell Fe_2O_3/Fe_2TiO_5 type II heterojunction and CoFe-PBA WOCs could be an effective approach to improve the PEC performance of photoanodes in acidic electrolytes, bringing new promise towards effective solar-fuel generation.

4. Experimental Section

Chemicals and Materials: All chemical reagents were purchased from Sigma-Aldrich and used without further purification. All solutions were prepared with Milli-Q water (ca. 18.2 MΩ·cm resistivity). Fluorine-tin-oxide (FTO) coated glass substrate (735167-1EA, 7Ω/sq) was purchased from Sigma-Aldrich and pre-cleaned before using as substrates.

FTO Pre-clean process: FTO substrates were cut into small pieces (area: 1 cm × 3 cm) and washed by sonicating in a (1 : 1 : 1) mixture of acetone (99.9%), isopropanol (99.9%) and water. After rinsing thoroughly with distilled water, the FTO substrates were washed in ethanol (Fluka, 99.8%) and then dried in air at 300 °C for 1 h (heating rate: 8.5 °C min^{-1}). Then, part of the FTO substrates (ca. 1 cm × 2 cm) was covered using a polymer tape (Kaptons® Foil, VWR International). The uncoated part of the FTO was later employed as electric contact for the working electrodes in the photoelectrochemical cell.

Fe_2O_3 electrodes: Hematite nanowires were prepared according to our previously published procedure.[38] Typically, a 200 ml Teflon-lined stainless-steel autoclave was filled with 60 ml aqueous mixture solution of 0.15 M ferric chloride ($FeCl_3$, 97%), 1 M sodium nitrate ($NaNO_3$, 99%) and 316 μL hydrochloric (HCl, wt 37%). 6 pieces of FTO substrates were put into the autoclave, which is sealed and heated at 95 °C for 4 hours. A homogenous layer of iron oxyhydroxide (FeOOH) nanowires was grown onto the FTO substrate. After that, the FeOOH coated FTO substrates was washed with deionized water to remove any residual salts, and subsequently pre-sintered in air at 550°C (heating rate: 8.5°C min^{-1}) for 2 hours to convert

FeOOH nanowires into hematite nanowires. To further reduce the surface defective sites and improve the crystallinity, the obtained hematite nanowires were post-sintered at 750 °C in air for additional 30 min and cooled down to the room temperature in 1 min.

Fe_2O_3/Fe_2TiO_5 electrodes: The obtained hematite samples after a pre-sintering process (550°C for 2h) were further subjected to an atomic layer deposition (ALD) TiO_2 process. The ALD TiO_2 was performed in a R200 Picosun Atomic Layer Deposition system at 150°C with $TiCl_4$ (99.9%) and water as the precursors in an 8 mbar N_2 flow atmosphere with a growth rate of 0.27Å $cycle^{-1}$. The pulse time for the $TiCl_4$ and water were 0.1 s and the purge time was 10 s. The thickness of TiO_2 coating onto the Fe_2O_3 nanowires can be controlled by changing the ALD deposition cycle. In this case, the optimized TiO_2 layer corresponds to 30 cycles according to our previous report.[38] After that, a post-sintering process at 750 °C for 30 min has been performed to transform the surface ALD TiO_2 into Fe_2TiO_5.[38, 54]

Fe_2O_3/Fe_2TiO_5/CoFe-PBA electrodes: The obtained Fe_2O_3/Fe_2TiO_5 electrodes were further coated with CoFe-PBA via chemical bath.[25] Chemical bath deposition of CoFe-PBA on the Fe_2O_3/Fe_2TiO_5 electrodes were carried out according to the following procedure: Firstly, $Co(NO_3)_2{\cdot}_6H_2O$ (700 mg) and $K_3Fe(CN)_6$ (350 mg) powder were dissolved in 40 mL of Milli-Q water under vigorous stirring. After that, one piece of Fe_2O_3/Fe_2TiO_5 electrodes was immersed in a 5 mL glass vial with 4 mL freshly prepared mixture solution containing $Co(NO_3)_2{\cdot}6H_2O + K_3Fe(CN)_6$. The glass vial was sealed and then heated at 60 °C for different reaction times in the oven. Finally, the obtained samples were rinsed with Milli-Q water to remove any impurities and were dried in the oven at 60 °C overnight.

Structural and morphological characterization: The grazing incidence X-ray diffraction (XRD) analyses were conducted on a Bruker D4 X-ray powder diffractometer via using the Cu Ka radiation (1.54184 Å) and a 1D Lynkeye detector, which is equipped with a Gobel mirror in the incident beam and equatorial Soller slits in the diffracted beam (51 incidence angle, 2° $step^{-1}$). The surface morphology of the electrodes was characterized via using a field

emission gun scanning electron microscope (FE-SEM, Zeiss Series Auriga microscopy) equipped with an electron dispersive X-ray spectroscopy (EDX) detector. X-ray photoelectron spectroscopy (XPS) was performed with a Phoibos 150 analyser (SPECS GmbH, Berlin, Germany)) in a ultra-high vacuum condition (base pressure 4×10^{-10} mbar) with a monochromatic aluminium K_α X-ray source (1486.74 eV). The energy resolution is 0.8 eV based on the FWHM measurement of the Ag $3d_{5/2}$ peak for a sputtered silver foil. Infrared absorption spectroscopy was performed with a ThermoScientific NICOLET iS50 Fourier transform infrared (FT-IR) spectrometer. Raman Spectrum was conducted at InVia-RENISHAW with incident wavelength: 514 nm. Optical properties of all electrodes were characterized by using a UV-vis spectrophotometer (Lambda 950, Perkin Elmer) equipped with an integrating sphere (150 mm diameter sphere covered with Spectralon as the reflecting material, Perkin Elmer). Absorbance (A) measurements were obtained from measured reflectance (R, %) and transmission (T, %), using a wavelength range of 350 to 800 nm and a step of 5 nm, respectively. All the samples for HRTEM and ADF-STEM were produced via using a mechanical process.[38] HRTEM and ADF-STEM images were obtained by using a FEI Tecnai F20 field emission gun microscope with a 0.19 nm point-to-point resolution at 200 kV equipped with an embedded Quantum Gatan Image Filter for EELS analyses. Atomic resolution AC HAADF STEM and further EELS-STEM analyses were conducted at a FEI TITAN 80-300 STEM operated at 300kV and a TITAN G3 50-300 PICO operated at 80kV.[59-60] Images were analyzed via using Gatan Digital Micrograph software. The Eje-Z, Rhodius and JMOL software packages were employed for the atomic supercell modelling with the corresponding crystal phase parameters of each species obtained from the Inorganic Crystal Structure Database (ICSD).[61-63] Specifically, to further identify the crystal phases via HRTEM, HAADF STEM and probe the spatial distribution of these components in the composite hematite electrodes, we created crystal models based on the single crystal data found in the ICSD. With these crystal models, the diffraction patterns visualized from

different zone axes of each species could be simulated. Then, the simulated diffraction pattern was compared with the power spectrum (FFT) obtained on the atomic resolution HRTEM and HAADF STEM experimental images for the identification of the crystal phases in the composite hematite electrodes.

Photo-electrochemical measurements: Photocurrent density (j, mA cm^{-2}) *vs.* applied potential (E, V) curves were conducted using a three-electrode cell. The working, counter and reference electrodes were the composite hematite photoanodes (1 cm^2 geometric area), a Pt wire and an Ag/AgCl (3 M KCl) reference electrode (Metrohm, E = 0.203 *vs.* NHE), respectively. The utilized electrolyte was a 0.1 M $NaNO_3$ + 0.1 M HNO_3 solution (pH=1), which was purged with N_2 during the experiments. CV was taken using a computer-controlled potentiostat (VMP3, BioLogic Science Instruments). CV scan was from 0.30 V vs. Ag/AgCl to 1.60 V vs. Ag/AgCl, with a scan rate of 20 mV s^{-1}. The photocurrent density is calculated based on the geometric area. All potentials were corrected at 80% for the ohmic drop, which was determined using the automatic current interrupt (CI) method implemented by the potentiostat,[25] and are converted with respect to the reversible hydrogen electrode (RHE): E (V *vs.* RHE) = E (V *vs*. Ag/AgCl) + 0.0592×pH + 0.203. Light illumination calibration was performed using a 150 W AM 1.5G solar simulator (Solar Light Co., 16S-300-002 v 4.0) with an incident light intensity set at 1 Sun illumination (100 mW cm^{-2}), as measured via using a thermopile (Gentec-EO, XLPF12-3S-H2-DO) coupled with an optical power meter (Gentec-EO UNO). In the PEC characterization, the light came from the front side (hematite-electrolyte interface, front side illumination). All the electrodes have been repeated at least three times, and the statistical photocurrent response data at 1.23 V vs RHE. are included in the supplementary information.

Faradaic efficiency measurement: The O_2 generated under chronoamperometric conditions (1.23 V vs RHE) during 2h and under 1 Sun illumination was measured with the calibrated Fibox detector immersed in the electrolyte in a gastight cell. The oxygen evolution

efficiencies were determined from the total amount of charge Q (C) passed through the cell. Assuming that four holes are needed to produce one O_2 molecule, the theoretical yield can be calculated as follows:

$$n_{O_2} = \frac{Q}{4F} \quad (4)$$

where F is the Faraday constant. The total mole of oxygen produced was quantitatively determined by using a calibrated Fibox detector with a temperature sensor.

Incident Photon to Current Efficiency (IPCE) was characterized using a xenon light source (Abet 150 W Xenon Lamp) coupled with a monochromator (Oriel Cornerstone 260 1/4 m monochromator). The wavelength was scanned from 350 to 800 nm (step: 10 nm $step^{-1}$) keeping the voltage fixed at 1.23 V vs. RHE. IPCE was calculated based on the following equation:[38]

$$IPCE\ (\%) = (1240/\lambda) \times (I/J_{light}) \times 100 \quad (5)$$

Where I is the photocurrent density (mA cm^{-2}) obtained using a potentiostat recording the i-t curve at 1.23 V vs. RHE, λ is the incident light wavelength (nm) from monochromatic, and J_{light} (mW cm^{-2}) is the power density of monochromatic light at a specific wavelength. A source meter (Keithley Instruments Inc., model no. 2400) coupled with the standard Silicon Photodiode (Thorlabs, S120VC) was used to measure the power density of monochromatic light.

PEIS data were obtained with an alternate current (AC) perturbation of 5 mV in amplitude and a 100 mHz to 10^5 Hz frequency range, both in the dark and under illumination, and under selected direct current (DC) potentiostatic conditions (0.30 to 1.60 V *vs.* Ag/AgCl). Nyquist plots (imaginary *vs*. real components of impedance, Z_{Im} *vs*. Z_{Re}) were fitted to the corresponding equivalent circuits via using Z-fit (BioLogic Associates). Fitted capacitances and resistances are calculated based on the electrode geometric area (1cm^2). Error bars are derived from the goodness of the EIS data fittings.

Supporting Information

Supporting Information is available from the Wiley Online Library or from the author.

Acknowledgements

This work was supported by the Spanish Ministerio de Economia y Competitividad (MINECO, grants CTQ2015-71287-R, CTQ2015-71287-R and CTQ2015-68770-R) and the coordinated Project ValPEC (ENE2017-85087-C3), the BIST Ignite Project inWOC2 and the Generalitat de Catalunya (2017 SGR 90, 2017 SGR 327, 2017 SGR 329, 2017 SGR 1246 and 2017 SGR 1406). ICN2 acknowledges the support from the Severo Ochoa Program (MINECO, Grant SEV-2017-0706). ICN2, ICIQ and IREC are funded by the CERCA Programme/Generalitat de Catalunya. P. Y. Tang acknowledges the scholarship support of DAAD short term grant. H. C. Du acknowledges support from the Deutsche Forschungsgemeinschaft (SFB 917). F. S. Hegner thanks the "LaCaixa"-Severo Ochoa International Programme (Programa internacional de Becas "LaCaixa"- Severo Ochoa) for a PhD fellowship. P. Paciok thanks for the support by the Bundesministerium für Bildung, und Forschung (Fundingregistration number: FK03ET6080E). We acknowledge Dr. Guillaume Sauthier from the ICN2 for the XPS measurements and Dr. Nina M. Carretero from IREC for the help in Faradaic efficiency measurement. Part of the present work has been performed in the framework of Universitat Autònoma de Barcelona Materials Science PhD program.

Received: ((will be filled in by the editorial staff))

Revised: ((will be filled in by the editorial staff))

Published online: ((will be filled in by the editorial staff))

References

[1] N. S. Lewis, *Science*, **2007**, *315*, 798-801.

[2] A. Fujishima, K. Honda, *Nature*, **1972**, *238*, 37-38.

[3] A. J. Bard, M. A. Fox, *Acc. Chem. Res*., **1995**, *28*, 141-145.

[4] K. Sivula, R. V. D. Krol, *Nat. Rev. Mater*., **2016**, *1*, 15010.

[5] V. Andrei, R. L. Z. Hoye, M. Crespo-Quesada, M. Bajada, S. Ahmad, M. D. Volder, R. Friend, E. Reisner, *Adv. Energy Mater*., **2018**, *8*, 1801403.

[6] S. X. Liu, L. X. Zheng, P. P. Yu, S. C. Han, X. S. Fang, *Adv. Funct. Mater.* **2016**, *26*, 3331-3339.

[7] X. Li, S. W. Liu, K. Fan, Z. Q. Liu, B. Song, J. G. Yu, *Adv. Energy Mater.* **2018**, *8*, 1800101.

[8] L. X. Zheng, S. C. Han, H. Liu, P. P. Yu, X. S. Fang, *Small*, **2016**, *12*, 1527-1536.

[9] W. X. Ouyang, F. Teng, J. H. He, X. S. Fang, *Adv. Funct. Mater.*, **2019**, *29*, 1807672.

[10] N. S. Lewis, *Nat. Nanotechnol.*, **2016**, *11*, 1010-1019.

[11] W. Li, S.W. Sheehan, D. He, Y.M. He, X.H. Yao, R. L. Grimm, G. W. Brudvig, D. W. Wang, *Angew. Chem. Int. Ed.* **2015**, *54*, 11428-11432.

[12] J. F. Zhang, R. García-Rodríguez, P. Cameron, S. Eslava, *Energy Environ. Sci.*, **2018**, *11*, 2972-2984.

[13] S. Chabi, K. M. Papadantonakis, N. S. Lewis, M. S. Freund, *Energy Environ. Sci.*, **2017**,*10*, 1320-1338.

[14] T. Reier, H.N. Nong, D. Teschner, R. Schlögl, P. Strasser, *Adv. Energy Mater.* **2017**, *7*, 1601275.

[15] J. R. McKone, N. S. Lewis, H. B. Gray, *Chem. Mater.* **2014**, *26*, 407-414.

[16] M. Blasco-Ahicart, J. Soriano-López, J. J. Carbó, J. M. Poblet, J. R. Galan-Mascaros, *Nat. Chem.*, **2018**, *10*, 24-30.

[17] Q. S. Yin, C. L. Hill, *Nat. Chem.*, **2018**, *10*, 6-7.

[18] T. Li, O. Kasian, S. Cherevko, S. Zhang, S. Geiger, C. Scheu, P. Felfer, D. Raabe, B. Gault, K. J. J. Mayrhofer, *Nat. Catal.*, **2018**, *1*, 300-305.

[19] R. Frydendal, E. A. Paoli, I. Chorkendorff, J. Rossmeisl, I. E. L. Stephens, *Adv. Energy Mater*. **2015**, *5*, 1500991.

[20] S. Kumari, B. P. Ajayi, B. Kumar, J. B. Jasinski, M. K. Sunkara, J. M. Spurgeon, *Energy Environ. Sci*., **2017**, *10*, 2432-2440.

[21] I. A. Moreno-Hernandez, C. A. MacFarland, C. G. Read, K. K. Papadantonakis, B. S. Brunschwig, N. S. Lewis, *Energy Environ. Sci.*, **2017**, *10*, 2103-2108.

[22] L. L. Zhao, Q. Cao, A. L. Wang, J. Z. Duan, W. J. Zhou, Y. H. Sang, H. Liu, *Nano Energy*, **2018**, *45*, 118-126.

[23] W. L. Kwong, C. C. Lee, A. Shchukarev, E. Björn, J. Messinger, *J. Catal.*, **2018**, *365*, 29-35.

[24] W. L. Kwong, C. C. Lee, A. Shchukarev, J. Messinger, *Chem. Commun*., **2019**, *55*, 5017-5020.

[25] L. J. Han, P. Y. Tang, Á. Reyes-Carmona, B. Rodriguez-Garcia, M. Torrens, J. R. Morante, J. Arbiol, J. R. Galan-Mascaros, *J. Am. Chem. Soc*., **2016**, *138*, 16037-16045.

[26] B. Rodríguez-García, A. Reyes-Carmona, I. Jiménez-Morales, M. Blasco-Ahicart, S. Cavaliere, M. Dupont, D. Jones, J. Rozière, J. R. Galán-Mascarós, F. Jaouen, *Sustain. Energy Fuels*, **2018**, *2*, 589-597.

[27] Y. Y. Zhao, K. R. Yang, Z. C. Wang, X. X. Yan, S. F. Cao, Y. F. Yei, Q. Dong, X. Z. Zhang, J. E. Thorne, L. Jin, K. L. Materna, A. Trimpalish, H. Y. Bai, S. C. Fakrai, X. Y. Zhong, P. Wang, X. Q. Pang, J. H. Guo, M. Flytzani-Stephanopoulos, G. W. Brudvig, V. S. Batistab, D.W. Wang, *Proc. Natl. Acad. Sci. USA*, **2018**, 201722137.

[28] W. Li, D. He, S. W. Sheehan, Y. M. He, J. E. Thorne, X. H. Yao, G. W. Brudvig, D. W. Wang, *Energy Environ. Sci.*, **2016**, *9*, 1794-1802.

[29] C. H. Cui, M. Heggen, W. D. Zabka, W. Cui, J. Osterwalder, B. Probst, R. Alberto, *Nat. Commun.*, **2017**, *8*, 1341.

[30] K. Sivula, F. L. Formal, M. Grätzel, *ChemSusChem*, **2011**, *4*, 432-449.

[31] K. G. U. Wijayantha, S. Saremi-Yarahmadi, L. M. Peter, *Phys. Chem. Chem. Phys.*, **2011**, *13*, 5264-5270.

[32] B. Klahr, S. Gimenez, F. Fabregat-Santiago, T. W. Hamann, J. Bisquert, *J. Am. Chem. Soc.*, **2012**, *134*, 4294-4302.

[33] A. J. Bard, A. B. Bocarsly, F. R. F. Fan, E. G. Walton, M. S. Wrighton, *J. Am. Chem. Soc.*, **1980**, *102*, 3671-3677.

[34] Y. B. Kuang, T. Yamada, K. Domen, *Joule*, **2017**, *1*, 290-305.

[35] S. Giménez, J. Bisquert, Photoelectrochemical solar fuel production-from basic principles to advanced devices, [M]. **2016**, Berlin: Springer.

[36] L. Steier, I. Herraiz-Cardona, S. Gimenez, F. Fabregat-Santiago, J. Bisquert, S.D. Tilley, M. Grätzel, *Adv. Funct. Mater.* **2014**, *24*, 7681-7688.

[37] F. S. Hegner, D. Cardenas-Morcoso, S. Gimenez, N. Lopez, J. R. Galan-Mascaros, *ChemSusChem*, **2017**, *10*, 4552- 4560.

[38] P. Y. Tang, H. B. Xie, C. Ros, L. J. Han, M. Biset-Peiró, Y. M. He, W. Kramer, A. Perez-Rodriguez, E. Saucedo, J. Galan-Mascaros, T. Andreu, J. R. Morante, J. Arbiol, *Energy Environ. Sci*, **2017**, *10*, 2124-2136.

[39] M. Itoi, T. Jike, D. Nishio-Hamane, S. Udagawa, T. Tsuda, S. Kuwabata, K. Boukheddaden, M. J. Andrus, D. R. Talham, *J. Am. Chem. Soc.* **2015**, *137*, 14686-14693.

[40] Y. H. Zhu, J. Ciston, B. Zheng, X. H. Miao, C. Czarnik, Y. C. Pan, R. Sougrat, Z. P. Lai, C. E. Hsiung, K. X. Yao, I. Pinnau, M. Pan, Y. Han, *Nat. Mater.*, **2017**, *16*, 532-536.

[41] D. L. Zhang, Y. H. Zhu, L. M. Liu, X. R. Ying, C. E. Hsiung, R. Sougrat, K. Li, Y. Han, *Science*, **2018**, *359*, 675-679.

[42] M. Martin-Sabi, J. Soriano-López, R. S. Winter, J.J. Chen, L. Vilà-Nadal, D. L. Long, J. R. Galán-Mascarós, L. Cronin, *Nat. Catal.*, **2018**, *1*, 208-213.

[43] S. Pintado, S. Goberna-Ferron, E. C. Escudero-Adan, J. R. Galan-Mascaros, *J. Am. Chem. Soc*, **2013**, *135*, 13270-13273.

[44] B. Klahr, T. Hamann, *J. Phys. Chem. C*, **2014**, *118*, 10393-10399.

[45] O. Zandi, T. W. Hamann, *J. Phys. Chem. Lett.*, **2014**, 5, 1522-1526.

[46] J. Suntivich, K. J. May, H. A. Gasteiger, J. B. Goodenough, S. H. Yang, *Science*, **2011**, *334*, 1383-1385.

[47] J. Li, R. Peat, L. Peter, *J. Electroanal. Chem. Interfacial Electrochem.*, **1984**, *165*, 41-59.

[48] O. Zandi, T. W. Hamann, *Nat. Chem.*, **2016**, *8*, 778-783.

[49] B. Iandolo, A. Hellman, *Angew. Chem. Int. Ed.* **2014**, *126*, 13622-13626.

[50] M. Sachsenhauser, I. D. Sharp, M. Stutzmann, J. A. Garrido, *J. Phys. Chem. C*, **2016**, *120*, 6524-6533.

[51] M. R. Nellist, F. A. L. Laskowski, J. J. Qiu, H. Hajibabaei, K. Sivula, T. W. Hamann, S. W. Boettcher, *Nat. Energy*, **2018**, *3*, 46-52.

[52] N. Yatom, O. Neufeld, M. C. Toroker, *J. Phys. Chem. C*, **2015**, *119*, 24789–24795.

[53] N. Yatom, Yuval Elbaz, S. Navona, M. C. Toroker, *Phys. Chem. Chem. Phys.*, **2017**, *19*, 17278-17286.

[54] D. M. Satoca, M. Bartsch, C. Fabrega, A. Genç, S. Reinhard, T. Andreu, J. Arbiol, M. Niederberger, J.R. Morante, *Energy Environ. Sci.*, **2015**, *8*, 3242-3254.

[55] T. L. Villarreal, R. Gómez, M. Neumann-Spallart, N. Alonso-Vante, P. Salvador, *J. Phys. Chem. B*, **2004**, *108*, 15172-15181.

[56] B. Klahr, S. Gimenez, F. Fabregat-Santiago, J. Bisquert, T. W. Hamann, *Energy Environ. Sci.*, **2012**, *5*, 7626-7636.

[57] K. G. Upul Wijayantha, S. Saremi-Yarahmadi, L. M. Peter, *Phys. Chem. Chem. Phys.*, **2011**, *13*, 5264-5270.

[58] E. A. Ponomarev and L. M. Peter, *J. Electroanal. Chem.*, **1995**, *397*, 45- 52.

[59] M. Heggen, M. Luysberg, K. Tillmann, FEI Titan 80-300 STEM, *Journal of large-scale research facilities*, **2016**, *2*, 42.

[60] J. Barthel, L. Houben, K. Tillmann, FEI Titan G3 50-300 PICO, *Journal of large-scale research facilities*, **2015**, *1*, 34.

[61] M. D.L. Mata, R. Leturcq, S. R. Plissard, C. Rolland, C. Magen, J. Arbiol, P. Caroff, *Nano Lett.*, **2016**, *16*, 825-833.

[62] S. Bernal, F. J. Botana, J. J. Calvino, C. Lopez-Cartes, J. A. Perez-Omil, J. M. *Ultramicroscopy*, **1998**, *72*, 135-164.

[63] R. R. Zamani, M. Ibanez, M. Luysberg, N. Garcia-Castello, L. Houben, J. D. Prades, V. Grillo, R. E. Dunin-Borkowski, J. R. Morante, A. Cabot, J. Arbiol, *ACS Nano*, **2014**, *8*, 2290-2301.

Figure 1. (A): 3D Atomic supercell models with solvent accessible surface illustrating the synthetic procedure for Fe_2O_3/Fe_2TiO_5/CoFe PBA photoanodes. SEM images of Fe_2O_3 (**B**), Fe_2O_3/Fe_2TiO_5 (**C**), and Fe_2O_3/Fe_2TiO_5/CoFe PBA (**D**) electrodes.

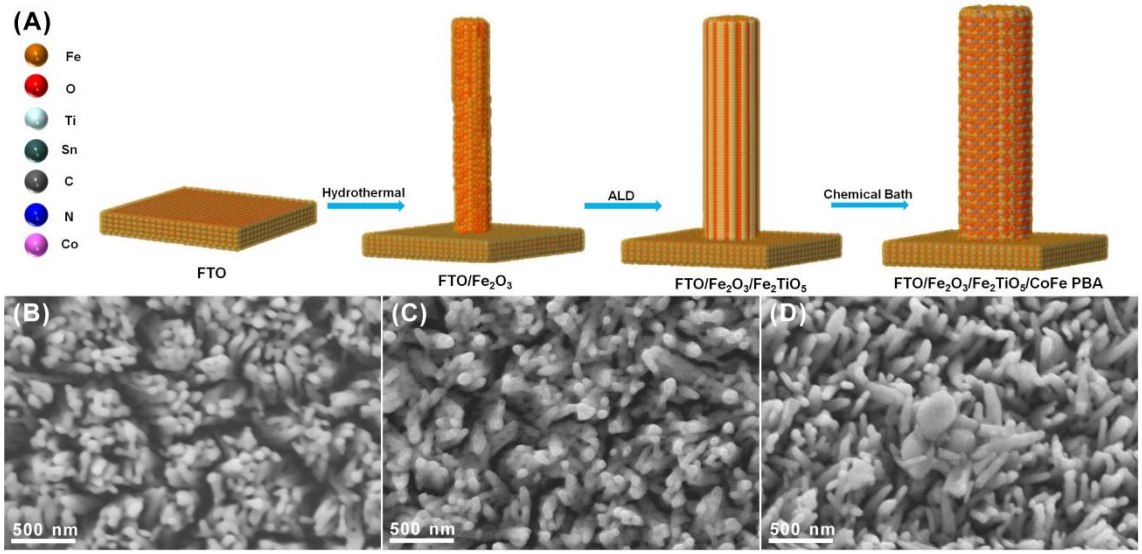

Figure 2. **Top row:** (Left) HAADF STEM image showing the atomic ordering at the edge region of the Fe_2O_3 electrode. (Middle) the corresponding colored FFT spectrum indicates that the nanowires crystallize in the hematite phase as visualized along the [2-21] direction. (Right) Atomic resolution HAADF STEM image of the green squared region showing the ordering of Fe, while O atoms are almost not visible in HAADF STEM mode due to the their weak Z-contrast. **Middle row:** (Left) HAADF STEM image showing the atomic ordering at the edge region of the Fe_2O_3/Fe_2TiO_5 electrode. (Middle) The corresponding colored FFT spectrum indicates that the nanowires matrix is hematite as visualized along the [2-21] direction. (Right) Atomic resolution HAADF STEM image of the blue squared region showing the typical ordering of Fe atoms in hematite. On the other hand, the Fe_2TiO_5 shell is observed as a blurred ultrathin shell (ca. 1 nm) on the surface of the hematite matrix since the height of hematite-core and Fe_2TiO_5 shell are different. (The inset shows the atomic model of Fe and O atoms visualized from the [2-21] direction, with Fe atoms marked as red and O atoms marked as green). **Bottom row:** (A): low magnification bright field TEM images showing the general morphology of the Fe_2O_3/Fe_2TiO_5/CoFe-PBA nanowires. (B): HRTEM detail showing the yellow squared interface area in (A). (C): Magnified HRTEM detail of the selected surface nanoparticle and (**D**): corresponding power spectrum indicating that the nanoparticle attached to the nanowire matrix crystallized in the cubic CoFe-PBA phase, as visualized along the [1-11] direction. (E): HRTEM image of the nanowire surface region squared in purple in (B). The white dotted line is marking an amorphous CoFe-PBA region. (F): Corresponding power spectrum (FFT) indicating that the nanowire heterostructure is mainly composed of hematite and pseudobrookite as visualized along the [-441] and [001] directions, respectively. (G): Frequency filtered structural map of the hematite (red) and pseudobrookite (green), showing their atomic stack sequence.

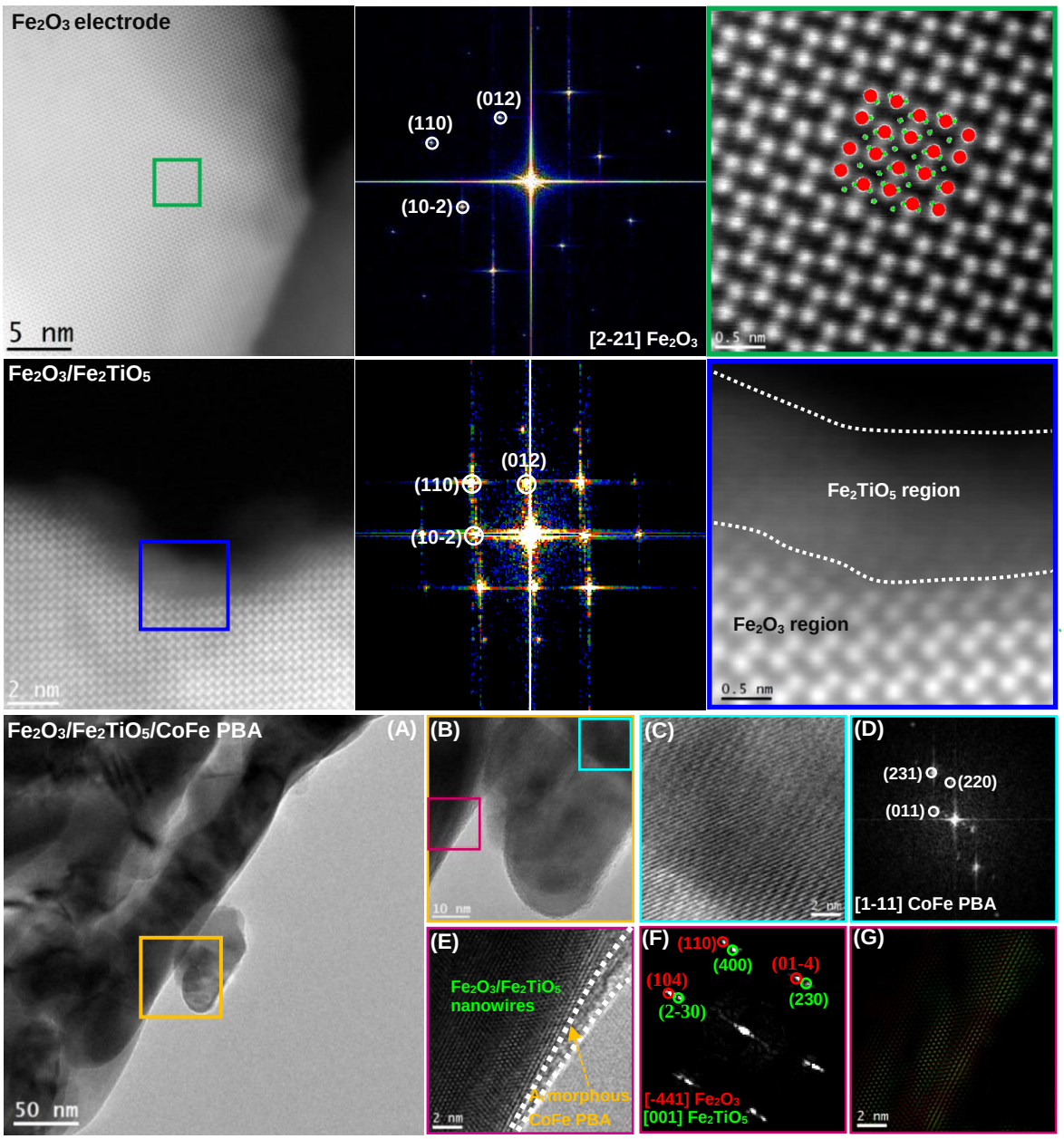

Figure 3. High magnification EELS chemical composition maps obtained from the blue rectangled area in the ADF-STEM micrograph of a nanowire extracted from the Fe_2O_3/Fe_2TiO_5/CoFe-PBA electrode. Individual Fe (red), C (green), Sn (blue), N (purple), Ti (indigo) and Co (yellow) maps and their composites.

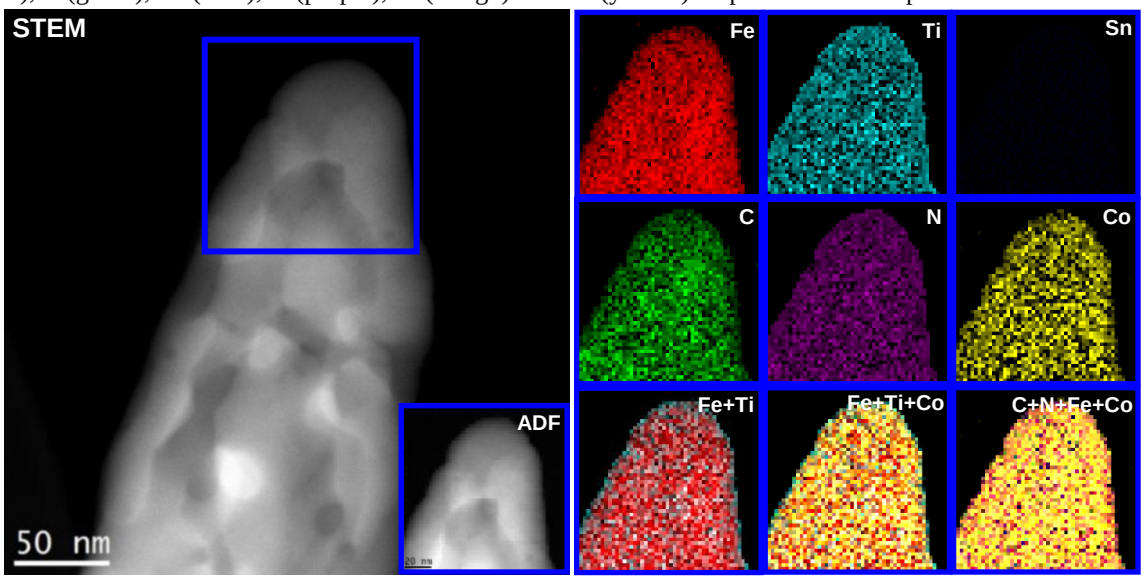

Figure 4. (**A**) Cyclic voltammetry under dark, (**B**) Cyclic voltammetry under illumination, (**C**) chopped light photocurrent-potential curves, and (**D**) photoelectrochemical stability test operated at 1.23 V *vs.* RHE of the Fe_2O_3, Fe_2O_3/Fe_2TiO_5, and Fe_2O_3/Fe_2TiO_5/CoFe-PBA electrodes for 24h. All polarization potentials reported here are relative to the reversible hydrogen electrode (RHE), and current densities is based on the geometric area. J (mA cm^{-2}) represents the current density response under light illumination. (**E**) Zoom in view of the atomic supercell model with solvent accessible surface of Fe_2O_3, Fe_2O_3/Fe_2TiO_5, and Fe_2O_3/Fe_2TiO_5/CoFe-PBA nanowires show the modified surface interfaces.

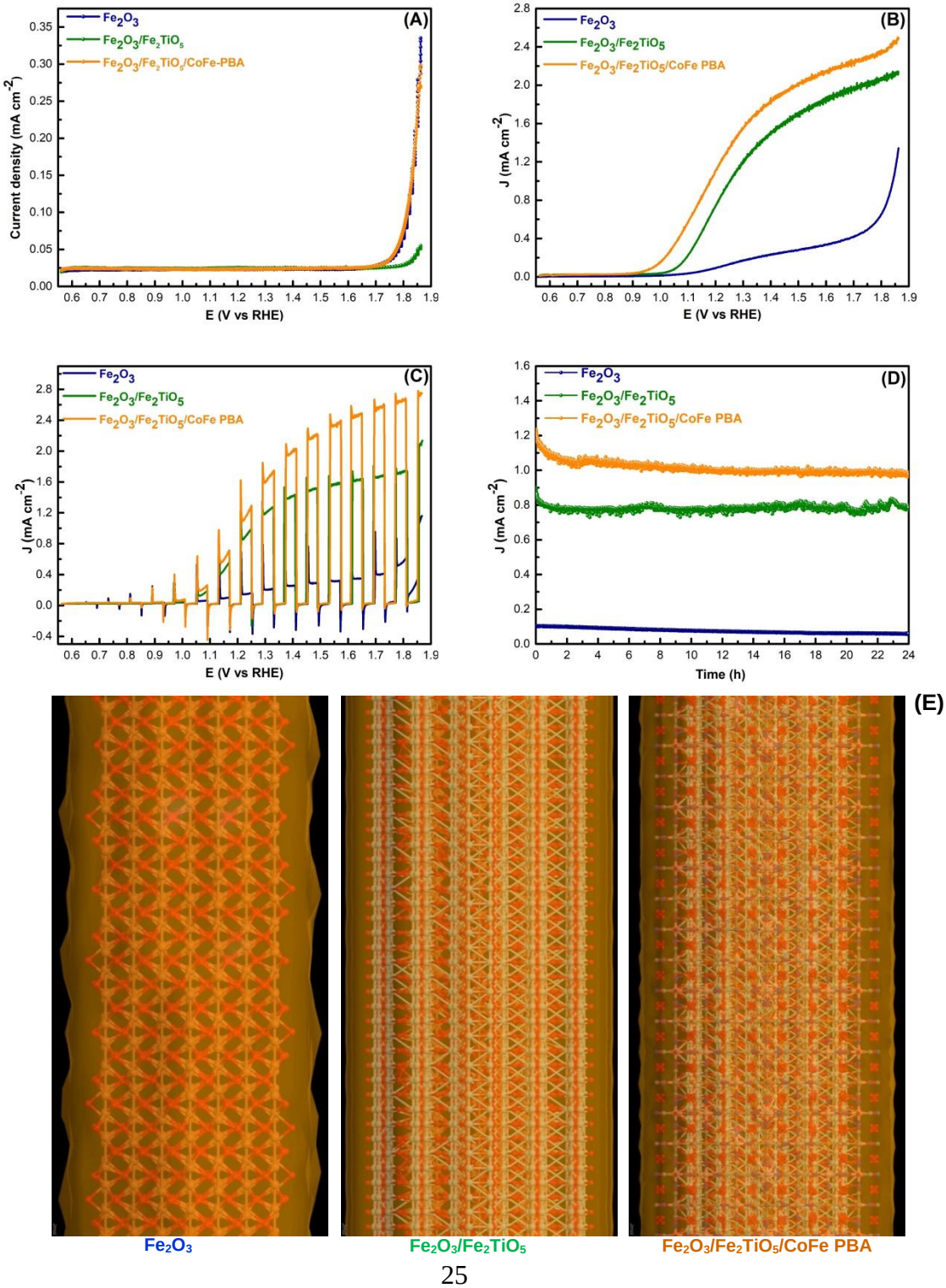

Figure 5. (**A**): CV curves scanned immediately in dark at 20 mV s^{-1} after holding the electrode potential at 1.85 V *vs*. RHE. for 1 min under illumination. (The inset shows its magnified plot). (**B**): Density of surface states (DOSS) as a function of the applied potential. Error bars stem from the goodness of the EIS data fittings. (**C**) Kinetic scheme of the charge generation and transfer processes at SEI at 1.23 V *vs*. RHE under illumination of these electrodes. Green and white areas represent electron filled and empty states, respectively. The dotted lines marked region in the CB filled states refer to photogenerated electrons with the same relative area as the empty states at the VB; the exceeding green regions highlight the doping levels in these electrodes. The green arrows denote the charge generation process upon photons absorption; the yellow arrows denote the hole trapping process at SS (surface states); the red arrows denote the hole transfer process from SS to electrolyte; the purple arrows denote to electron transfer from CB states to the FTO substrates. The thickness and shape of the arrows reveal the relative rates of the charge transfer processes, where the dotted lines mean the slowest rate (Fe_2O_3 electrode) and the thickest lines means the fastest rate (Fe_2O_3/Fe_2TiO_5/CoFe-PBA electrode). The light indigo shaded areas refer to the relative overlapping of the DOSS and water density of states. E: electrode potential; $E_{c,s}$: surface CB edge potential; E_F: Fermi level of the semiconductors that matches the electrode potential (E) and the O_2/H_2O couple thermodynamic potential (1.23 V *vs*. RHE); E_{SS}: center potential of the SS distribution; $E_{v,s}$: surface VB edge potential; λ: redox couple reorganization energy. It is worth noting that the relative size of the DOSS distribution for these electrodes has been intentionally enlarged to highlight the SS. (**D**): Total surface state density (N_{ss}), donor density (N_d), and their ratio (N_{ss}/N_d) plot. N_d was estimated from the slopes of the Mott-Schottky plots (Figure S30), whereas N_{ss} was obtained from integration of the DOSS profiles. Color bar with a unit of μm is plotted at the right Y axis for N_{ss}/N_d. (**E**): Ratio of the charge transfer rate constant (k_{ct}) and the sum of k_{ct} and trapping rate constant ($k_{trapping}$) at different potential.

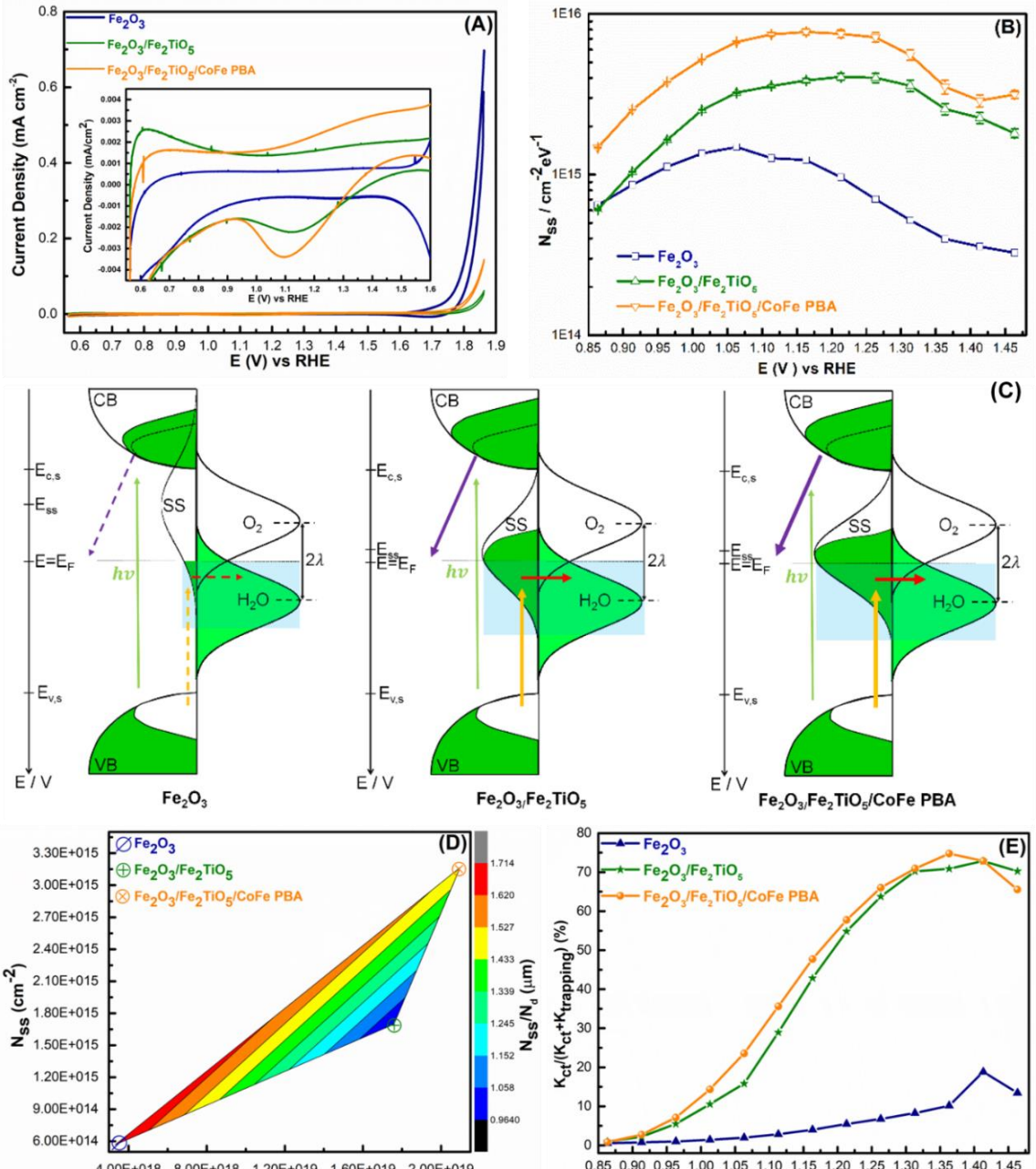

The table of contents

Detailed understanding of the semiconductor/electrolyte interface is critical to further development of photoelectrodes for photoelectrochemical water splitting. We find that modifying the hematite/electrolyte interface with ultrathin Fe_2TiO_5 and CoFe PBA improved the photoelectrochemical water oxidation of hematite photoanodes in acidic electrolyte. The modified hematite/electrolyte interface altered the surface states at hematite photoanodes, and thus improved the surface water oxidation kinetics.

Keyword

photoelectrochemical water splitting, hematite, surface states, acidic electrolyte.

Boosting Photoelectrochemical Water Oxidation of Hematite in Acidic Electrolytes by Surface States Modification